Calcination-Induced Oxygen Vacancies Enhancing the Photocatalytic Performance of a Recycled Bi_2O_3/BiOCl Heterojunction Nanosheet

Peng Li, Jie Qu, Jing Wu, Jie Zhang, Guoli Zhou, Ying Zhang, Yijun Cao, and Daoguang Teng*

Read Online

ACCESS | Metrics & More | Article Recommendations | SI Supporting Information

ABSTRACT: With the rapid development of industry, bismuth-based semiconductors have been widely used for the photocatalytic degradation of organic contaminants discharged into wastewater. Herein, a Bi_2O_3/BiOCl (BBOC) heterojunction was constructed with high photocatalytic activity toward Rhodamine B (RhB) in the first cycle of the photocatalysis test, while the photocatalytic performance was drastically reduced after repeated testing. The adsorbed RhB molecules occupying the facial active sites of BBOC contributed to the decline of photocatalytic activity. The spent BBOC can be reactivated by the decomposition of the adsorbed RhB and the introduction of oxygen vacancies during calcination under an air atmosphere. The BBOC thus recovered exhibited a superior apparent rate constant of 0.08087 min^{-1} compared with 0.05228 min^{-1} of pristine BBOC. This study provided an effective strategy to investigate the deactivation/activation mechanism of bismuth-based heterojunction photocatalysts.
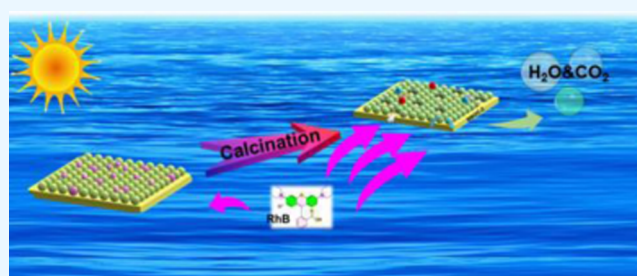
1. INTRODUCTION

Photocatalytic degradation has attracted increasing attention to settle organic contaminants discharged into wastewater for its environmentally friendly and complete mineralization process.[1−3] Bismuth-based semiconductor photocatalysts featuring nontoxicity and low cost have been widely investigated recently.[4] Specifically, tetragonal martensite BiOCl (BOC) with a $[Bi_2O_2]^{2+}$ sheet interlaced by two Cl layers[5,6] is regarded as a promising photocatalyst that provides sufficient space for polarization-dependent orbitals and atoms. The electrostatic field perpendicular to $[Bi_2O_2]^{2+}$ and $[Cl_2]$ lamellae inside BOC contributes to effective anticharging recombination and broadens the prospects of photocatalysis.[7,8] However, a wide bandgap (~3.5 eV) and high photocarrier recombination lead to the excitation of BOC only in the ultraviolet light region, significantly limiting its practical applications. Construction of heterojunctions (e.g., p−n,[9,10] Z-scheme,[11−13] and step-scheme heterojunctions[14−16]) is considered as an alternative to mitigate the inefficient charge separation and poor photocatalytic behavior. Therefore, combining BOC with narrow-bandgap bismuth-based semiconductors (e.g., Bi_2O_3 (BO)) to enhance the photocatalytic activity of composite materials is highly desired.[17−20]

Inspired by the abovementioned ideas, we prepared an efficient Bi_2O_3/BiOCl (BBOC) heterojunction with high photocatalytic performance toward organic contaminants via a facile solution reaction. However, the declined reaction activity of the recovered photocatalyst greatly diminished its commercial value due to the deactivation.[21−23] Photocatalyst

deactivation originated mainly from the adsorption of intermediates/byproducts onto the photocatalyst surface, blocking and thus losing the photocatalytic active sites.[24,25] Frequent replacement of deactivated catalysts contributed to an increased overall cost, thus necessitating investigations on the prevention of photocatalyst deactivation and/or activation of the deactivated catalysts. Recently, many strategies, including the construction of heterojunctions, surface modification, and oxygen vacancies (OVs), have been developed to activate deactivated photocatalysts.[26−28] In particular, OV construction was considered to be a facile alternative for activating deactivated photocatalysts compared with other strategies demanding modified or grafted additives. Remarkably, the construction of OVs via calcination can activate deactivated photocatalysts by accelerating the decomposition of the adsorbed contaminants at the same time.[29] The introduced OVs effectively adjusted the electronic structure and carrier concentration and extended the light absorption to longer wavelengths, thus facilitating the photogenerated carrier capture to hinder electron−hole pair recombination.[30−32] However, as far as we know, few investigations have focused on the deactivation and activation mechanism of BBOC

heterojunctions during photocatalytic degradation of organic contaminants. Hence, studies on activating deactivated BBOC heterojunctions to extend the life of catalysts are highly desired.

Under these circumstances, we used recovered BBOC (BBOC-1), which degraded 94.44% of Rhodamine B (RhB) with a concentration of 20 mg L^{-1} in 40 min in the first run of photocatalytic degradation and deactivated in the second run of the photocatalytic test, as target photocatalysts to investigate the activation route. BBOC-2 was obtained by calcining BBOC-1 at 350 °C under an air atmosphere and showed enhanced photocatalytic performance compared with that of BBOC and BBOC-1 according to the combined analytical characterization. After a detailed discussion, it was concluded that the adsorbed RhB was the core factor that determined the photocatalytic activities of BBOC-1 and BBOC-2. OVs appeared in BBOC-2 after activation by calcinating and contributed to the enhancement of photocatalytic performance. This study verified the new route for the introduction of OVs via facile calcination, which greatly enhanced the separation efficiency of photoinduced charge carriers, providing a reference with deep insights into the activation of deactivated photocatalysts.

2. EXPERIMENTAL SECTION

2.1. Materials. Bi(NO$_3$)$_3$·5H$_2$O, NaCl, and RhB were provided by Shanghai Aladdin Biochemical Technology Co., Ltd. (Shanghai, China). Concentrated HNO$_3$ (63 wt %), concentrated NH$_3$·H$_2$O (28 wt %), and ethanol (C$_2$H$_5$OH) were provided by Sinopharm Chemical Reagent Co. Ltd. (Shanghai, China). Deionized water (DIW) was homemade in the laboratory. All reagents were used as received without any further purification.

2.2. Catalyst Preparation. All catalysts were prepared based on our previous investigations and literature with some modifications.[19,33−35]

2.2.1. Preparation of BO. A concentrated HNO$_3$ solution (4 mL, 63 wt %) was added dropwise into a round-bottom flask (100 mL) containing DIW (50 mL) and Bi(NO$_3$)$_3$·5H$_2$O (12.000 g) under ultrasonication to achieve full dispersion. A certain amount of NH$_3$·H$_2$O was added to the mixture until the solution reached pH 7 under vigorous stirring (500 rpm) at room temperature and then reacting at 80 °C for 10 h. The Bi-containing precursor was obtained by filtering the light-orange suspension. BO was finally prepared by calcination in a tube furnace under an air atmosphere at 500 °C for 2 h with a heating rate of 3 °C min^{-1}.

2.2.2. Preparation of BBOC. NaCl (0.412 g) was added into a conical flask (250 mL) charged with DIW (100 mL) under magnetic stirring for 10 min to achieve complete dissolution. A certain amount of concentrated HNO$_3$ solution (63 wt %) was used to adjust the solution to pH 1, followed by magnetic stirring for 30 min. Then, the as-prepared BO (1.640 g) was added to the reaction solution and reacted under vigorous stirring (500 rpm) at room temperature for 3 h. Finally, the BBOC composite catalyst was filtered, washed with DIW several times, and dried at 60 °C for 12 h in vacuum.

2.2.3. Preparation of BOC. BOC was prepared via the same strategy as BBOC (eq 1),[18] except for changing the amount of added BO from 1.640 to 0.820 g.

$$Bi_2O_3 + 2H^+ + 2Cl^- = 2BiOCl + H_2O \qquad (1)$$

2.3. Photocatalyst Recovery and Activation. BBOC was recovered from the reaction solution after photocatalytic degradation of RhB. BBOC-1 was obtained by washing the filtration residue with DIW three times followed by drying at 60 °C for 12 h. BBOC-2 was obtained by calcining BBOC-1 at 350 °C for 2 h under an air atmosphere at a heating rate of 3 °C min^{-1}, with a yield of 70%.

2.4. Characterization. Scanning electron microscopy (SEM, SU8010, 30 kV, Hitachi) and transmission electron microscopy (TEM, JEM-2100F, 200 kV, JOEL) were used to observe the morphology and microstructure of the catalysts. Specific surface areas were analyzed at 77 K using the Brunauer−Emmett−Teller (BET) method using a Micromeritics analyzer (Auto-sotrb-IQ2-MP-XR). A powder X-ray diffractometer (XRD, Cu Kα source, Bruker, Karlsruhe, Germany) was used to analyze the physical phase and crystalline structure of the catalysts. The elemental or chemical composition of the catalyst surface, valency, and surface energy state distribution were characterized by X-ray photoelectron spectroscopy (XPS, VG Scientific Co., U.K.) analysis, where the C 1s peak (284.8 eV) was used to calibrate the binding energy. Ultraviolet−visible (UV−vis) diffuse reflectance spectroscopy (DRS, UV-3600, Shimadzu, Kyoto, Japan) was used to examine the photophysical properties of the samples, and the range of scanning was 200−800 nm. BaSO$_4$ was used as the reflectance standard. Thermogravimetry−differential scanning calorimetry (TG−DSC, NE-TZSCH STA 449F3) was employed to test the thermal stability of the samples in the range of 30−900 °C with a heating rate of 10 °C min^{-1}. Electron paramagnetic resonance spectrometry (EPR, Bruker A300, Germany) was used to confirm the existence of OVs in the photocatalysts.

2.5. Photocatalytic Experiment. A 300 W xenon lamp with a 400 nm cutoff filter was adopted as the visible-light source and was located 10 cm above reaction vessels in the following photocatalytic experiment. RhB was used as the target pollutant to test the photocatalytic performance of the as-prepared catalysts. A certain amount of the photocatalyst (20 mg) was dispersed in RhB solution (100 mL, 20 mg L^{-1}) under magnetic stirring for 30 min to achieve adsorption/desorption balance in the dark, and 3 mL of the suspended sample was taken at the end of the dark treatment and filtered through a 0.22 μm aqueous filter tip. The photocatalytic degradation tests were carried out at room temperature and pH = 5.5 with the light source turned on, and 3 mL of suspension samples were taken every 10 min during the experiments and filtered through a 0.22 μm aqueous filter tip. All of the obtained samples were measured using a UV−vis spectrophotometer to determine the degradation efficiency of the samples toward RhB solution. Intermediates of photocatalysis were detected by liquid chromatography−mass spectrometry (LC−MS, Ultimate 3000 UHPLC-Q Exactive) in the electrospray ionization (ESI) positive ion mode.

The degradation rate (D_t) of the pollutant was calculated using eq 2[36]

$$D_t = (c_0 - c_t)/c_0 \times 100\% = (A_0 - A_t)/A_0 \times 100\% \qquad (2)$$

where c_0 is the concentration of RhB solution before light irradiation, c_t is the concentration of RhB solution at moment t, A_0 is the absorbance of RhB solution before light irradiation, and A_t is the absorbance of RhB solution at moment t.
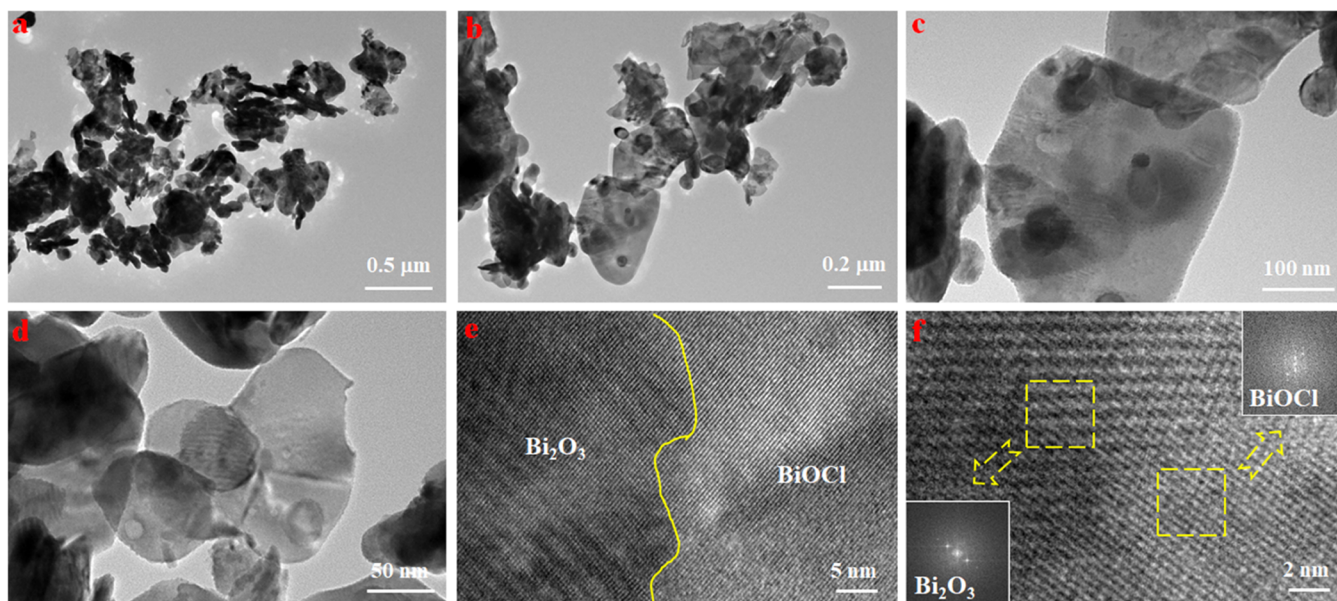
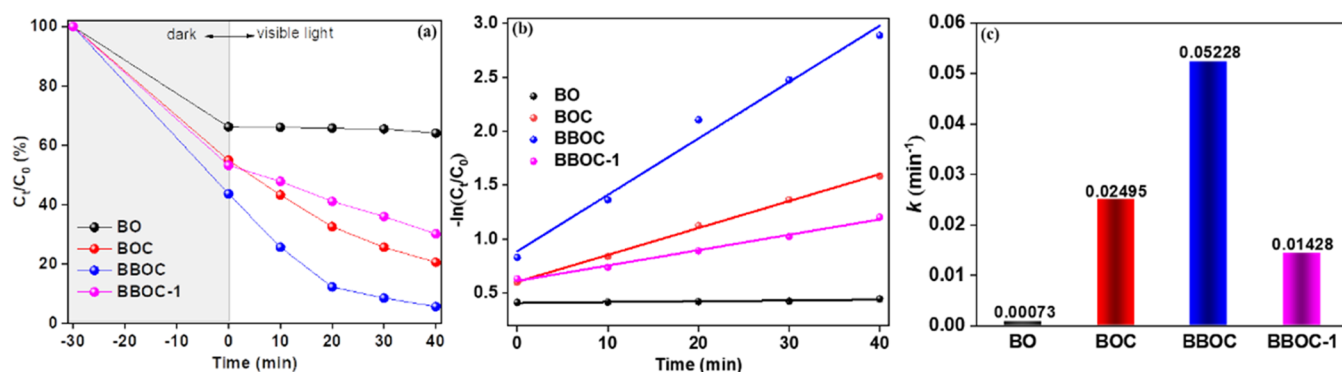**Figure 1.** (a–d) TEM and (e, f) high-resolution TEM (HRTEM) images of BBOC.

Figure 2. (a) Photocatalytic degradation performances of RhB using BO, BOC, BBOC, and BBOC-1, respectively. (b) Linear fitting of the pseudo-first-order kinetic equation. (c) Histogram of the apparent rate constant k.
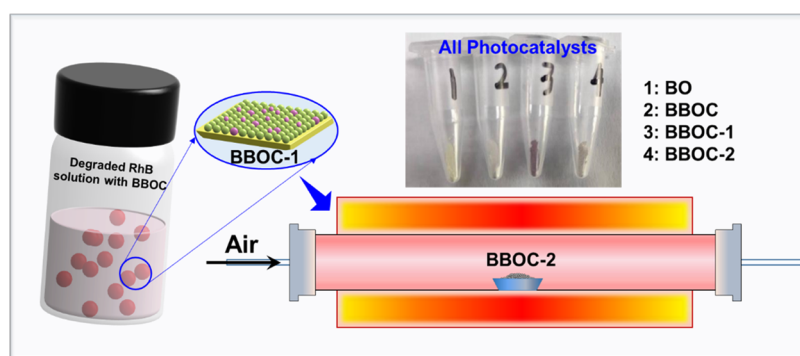

Figure 3. Schematic diagram of the BBOC-1 activation process.

3. RESULTS AND DISCUSSION

3.1. Photocatalytic Performance of the Heterojunction. BBOC was prepared successfully according to the basic physical property characterizations in our previous investigations via the aforementioned preparation route. TEM and HRTEM images (Figure 1) revealed the microstructure of the BBOC heterojunction. As shown in Figure 1a–d, nanosheets are tightly bound, shaped like slices growing from the substrate. More specifically, the HRTEM images of BBOC

(Figure 1e,f) present a clear crystal plane spacing, in which the lattice fringes with d-spacings of 0.33 and 0.74 nm correspond to the (120) plane of BO and the (001) plane of BOC, respectively.[37,38] It is apparent that the BBOC heterojunction was fabricated by the in situ construction of BOC on the BO surface.

BBOC was confirmed as an effective photocatalyst according to the degradation tests (Figure S1). As can be seen from Figure 2a, BBOC degraded 94.44% of the RhB in 40 min
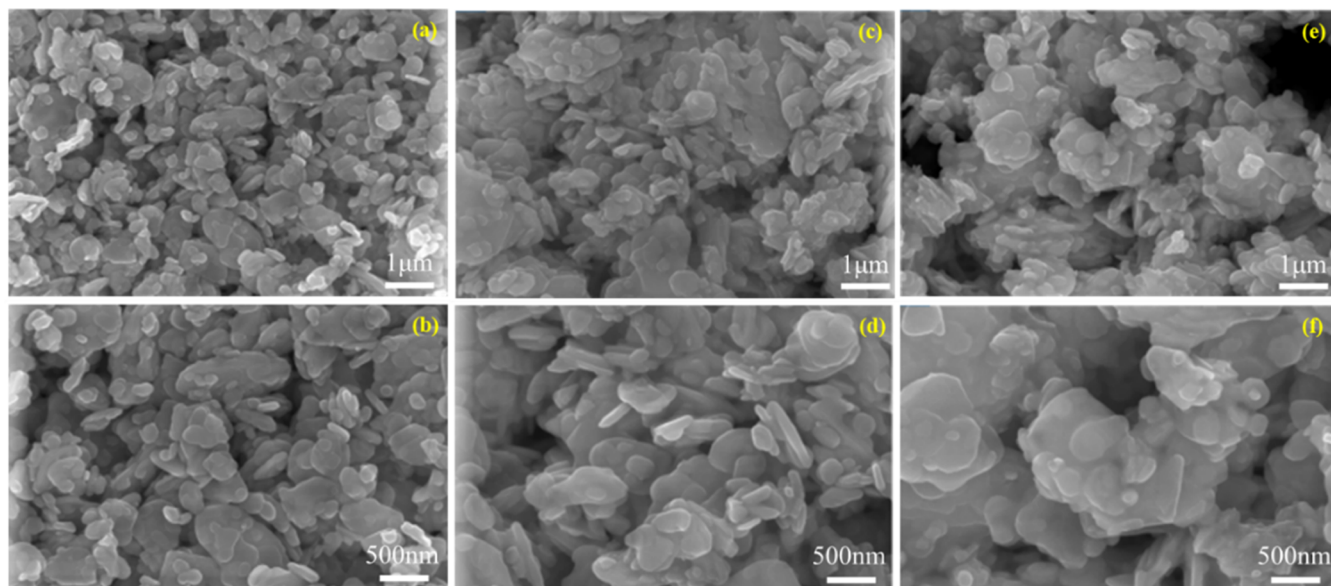
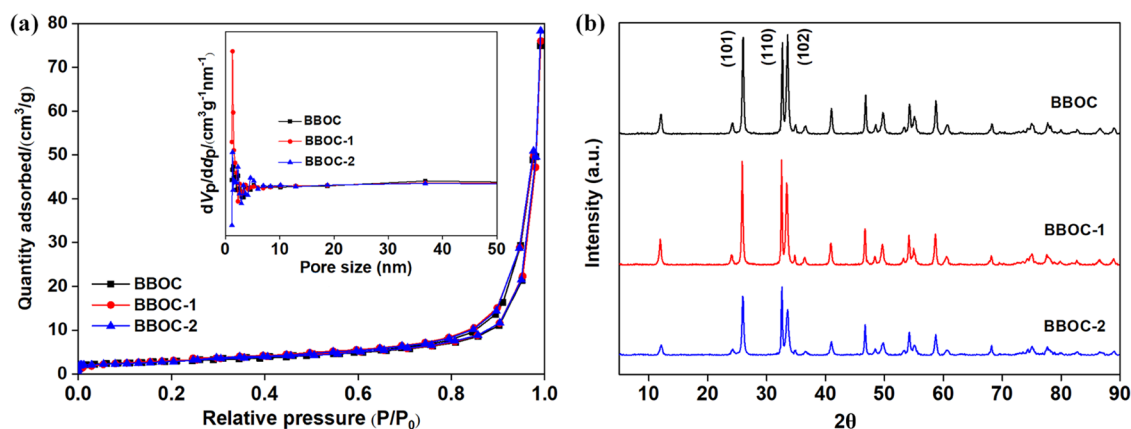**Figure 4.** SEM images of (a, b) BBOC, (c, d) BBOC-1, and (e, f) BBOC-2.

Figure 5. (a) N$_2$ adsorption−desorption curves and BJH pore size distributions (inset). (b) XRD patterns of BOC, BBOC-1, and BBOC-2.

under UV−vis light irradiation, which was significantly higher than that of BO (35.96%) and BOC (79.5%). RhB cannot be degraded without any photocatalyst even under light irradiation. The heterojunction structure of BBOC led to considerable enhancement of photocatalytic performance. However, BBOC-1 exhibited much lower reaction activity, with only 46.81% adsorption in the dark and 69.97% total removal rate of RhB under the same reaction conditions. In addition, the pseudo-first-order kinetic model ($\ln(c_t/c_0) = kt$) was used to further describe RhB photodegradation, where k represented the kinetic constant, c_t and c_0 were the concentrations of RhB in aqueous solution at time t and 0, respectively.[39−41] The fitted kinetic model curves and the apparent rate constant k of the kinetic equation are illustrated in Figure 2b,c. BBOC possessed the maximum k value of 0.05228 min^{-1}, which is 3.7, 2.1, and 71.3 times higher than those BBOC-1 (0.01428 min^{-1}), BOC (0.02495 min^{-1}), and BO (0.00073 min^{-1}). Thus, the photocatalytic activity of BBOC-1 was greatly reduced after recovering and BBOC-1 needed activation for further utilization. The following part of this study focused on finding the reason for the deactivation of BBOC-1 and providing a solution to the activation of BBOC-1.

3.2. Properties of Photocatalysts. BBOC-2 was gained by calcining BBOC-1 at 350 °C under an air atmosphere, as shown in Figure 3 and all photocatalysts can be distinguished from their different colors as in the inset image. The as-prepared pure BO accumulated as a light-yellow powder, while BBOC became pale. BBOC-1 changed to dark red after the degradation of RhB, which was possibly due to the undegraded RhB dispersed in BBOC-1. The dark red color disappeared after calcination, and BBOC-2 became gray, suggesting the decomposition of the dark red substance. Characterizations of physical properties were conducted to reveal the transformation inside BBOC-2 during calcination.

Figure 4 shows the SEM images of BBOC, BBOC-1, and BBOC-2. BBOC was well accumulated, with uniform flakes without agglomeration, contributing to its excellent photocatalytic performance. The reduction of pores in BBOC-1 (Figure 4c,d) compared with that in BBOC (Figure 4a,b) resulted from the adsorption of small molecules during the photocatalytic degradation of RhB, which accounted for the dark red color of BBOC-1 after the first run of the photocatalytic reaction. BBOC-2 also displayed nanosheet accumulation but with obvious agglomeration (Figure 4e,f), indicating the occurrence of sintering during calcination.

However, larger pores that were conducive to contaminant adsorption were also generated in BBOC-2 at the same time, which would enhance the photocatalytic performance of BBOC-2.

The BET specific surface areas and Barrett−Joyner−Halenda (BJH) pore size distributions are shown in Figure 5a, and the detailed data are listed in Table 1. All samples

**Table 1. Porosity Properties of Photocatalysts**

sample	S_{BET} (m^2 g^{-1})	pore size (nm)	pore volume (cm^3 g^{-1})
BBOC	11.079	40.774	0.1129
BBOC-1	10.976	40.209	0.1103
BBOC-2	10.526	43.604	0.1148

exhibited characteristic type II isotherms with H3 hysteresis loops, indicating the existence of a large number of micropores.[42−44] As shown in Figure 5a, BBOC-1 possessed the most micropores with the smallest pore structures, BBOC-2 featured more mesopores, while BBOC was intermediate. These results were in good agreement with SEM observations. Considering the dark red color of BBOC-1, the decrease in BET specific surface areas and the same N$_2$ adsorption−desorption pattern as those of BBOC and BBOC-2 suggested that the adsorbed RhB was not thoroughly degraded and blocked part of the pores.

Figure 5b displays the XRD patterns of BBOC, BBOC-1, and BBOC-2. All three samples shared similar peaks, and no distinct differences appeared after recovering as well as activating BBOC, indicating good crystalline stability of the heterojunction composite catalysts. The characteristic peaks at $2\theta = 26.0$, 32.7, and 33.6° corresponded to (101), (110), and (102) planes of BBOC, respectively. Hence, the growth of the highly active (110) crystal plane enhanced the dye adsorption capacity and sensitization performance of BOC, which consequently resulted in the poor cycling performance of the composite catalyst.[45−47] That is to say, the high adsorption activity toward RhB and the blocking of internal pores by undecomposed RhB resulted in the low photocatalytic performance of BBOC-1.[48]

XPS was conducted to reveal the surface elemental compositions, chemical states, and electronic states of the samples.[49] Figure 6 shows the binding energy positions of all elemental peaks with correction for the C standard binding energy of 284.8 eV. BBOC, BBOC-1, and BBOC-2 were mainly composed of Bi, O, and Cl elements, as shown in Figure 6a, and no other elements were detected. The similar XPS peak patterns of BBOC, BBOC-1, and BBOC-2 were in good agreement with the XRD patterns. Bi 4f XPS spectra in Figure 6b display two peaks located at around 159.30 and 164.61 eV attributed to Bi 4f$_{7/2}$ and Bi 4f$_{5/2}$, respectively.[50] The Bi 4f binding energy of BBOC-2 shifted to a higher value with two satellite peaks (Sat.), proving the removal of small molecules as well as the enhanced interaction between substances during calcination.[51] In Figure 6c, the peak of O 1s located at lower binding energy (∼530 eV) was assigned to the Bi−O bond in the composite material, and the peak at higher binding energy (∼532 eV) could be attributed to the oxygen vacancies. The OV peak of BBOC-2 showed the strongest intensity, indicating the generation of OVs during calcination.[52−54] Compared with that of BBOC, RhB adsorption led to a decrease in the Cl 2p binding energy value of BBOC-1, while the decomposition of RhB via
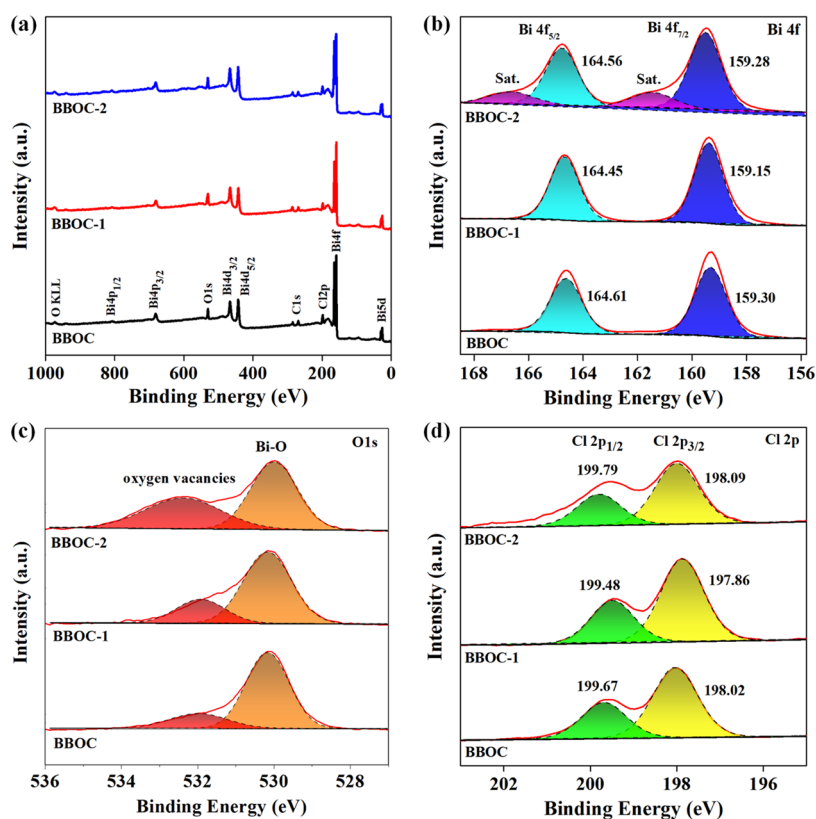
Figure 6. XPS spectra for BBOC, BBOC-1, and BBOC-2: (a) survey scan, (b) Bi 4f, (c) O 1s, and (d) Cl 2p.
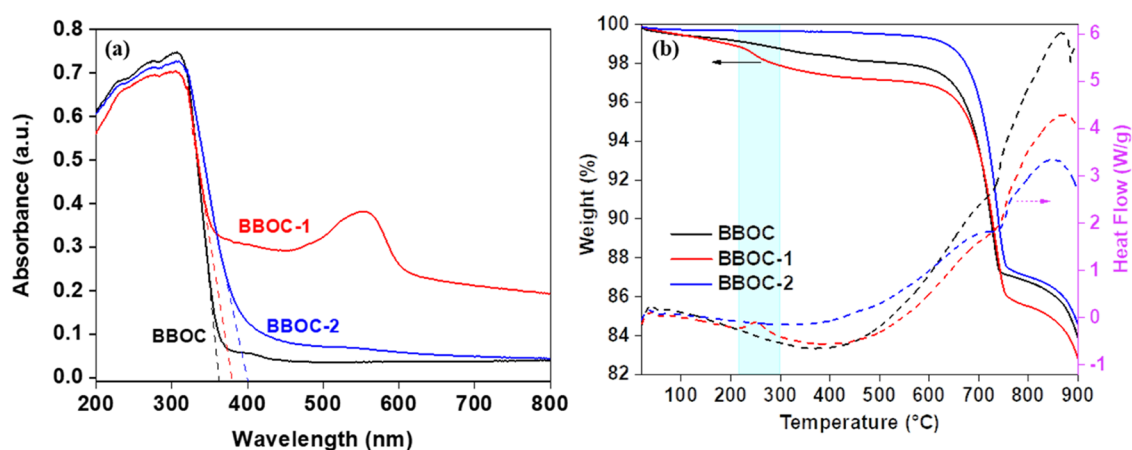
Figure 7. (a) Solid UV−vis DRS spectra. (b) TG-DSC curves of BBOC, BBOC-1, and BBOC-2.
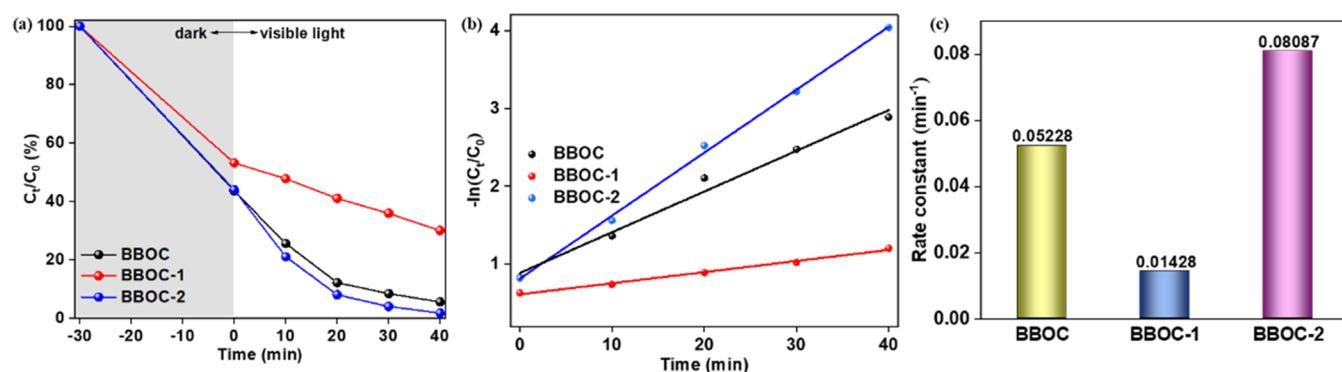

Figure 8. (a) RhB photocatalytic degradation curves. (b) Proposed first-order kinetic curves. (c) Apparent rate constant k using BBOC, BBOC-1, and BBOC-2 as photocatalysts, respectively.
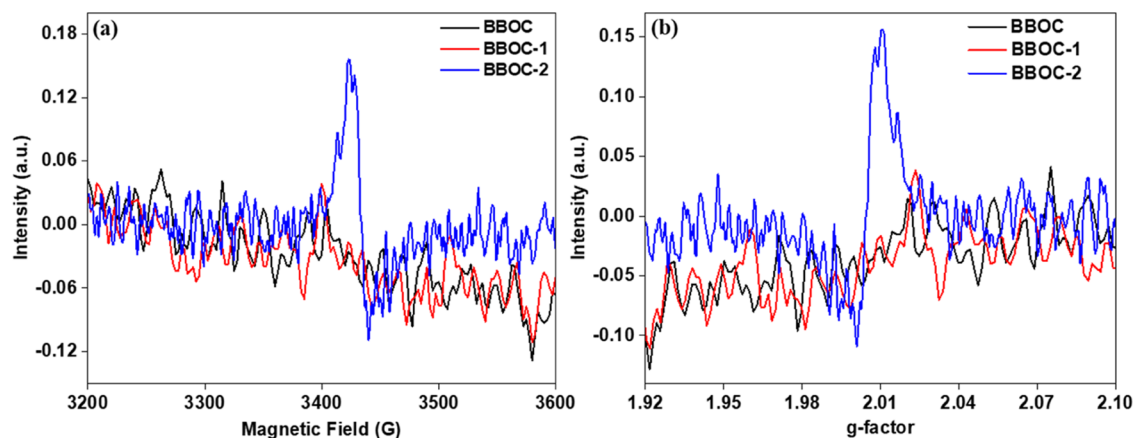

Figure 9. (a, b) EPR spectra of BBOC, BBOC-1, and BBOC-2.

calcination restored the Cl 2p binding energy of BBOC-2, as shown in Figure 6d.[45]

Figure 7a illustrates the optical absorption of BBOC, BBOC-1, and BBOC-2. BBOC exhibited absorbance only in the UV region, while BBOC-1 and BBOC-2 exhibited apparent absorption in the visible light region. As for BBOC-1, the red shift of the absorption edge was attributed to the strong absorption of visible light by RhB as a photosensitizer.[45] The new peak that appeared at around 564 nm in the curve of BBOC-1 was the characteristic absorption peak of RhB,[47] while the characteristic peak then disappeared in the curve of BBOC-2. The UV−vis DRS spectra provided more direct

evidence for the RhB adsorption in BBOC-1 as well as the RhB decomposition of BBOC-2. In addition, the red shift of the absorption edge would improve the light absorption capacity of BBOC-2.[52] The forbidden bandwidths of BBOC, BBOC-1, and BBOC-2 were calculated to be 3.44, 3.26, and 3.10 eV, respectively (eq S1).

TG-DSC curves (Figure 7b) provided more detailed descriptions of the differences among BBOC, BBOC-1, and BBOC-2. BBOC-1 displayed an exothermic peak at 250 °C, which was derived from RhB decomposition. As for BBOC and BBOC-2, no obvious weight loss appeared at around 250 °C,
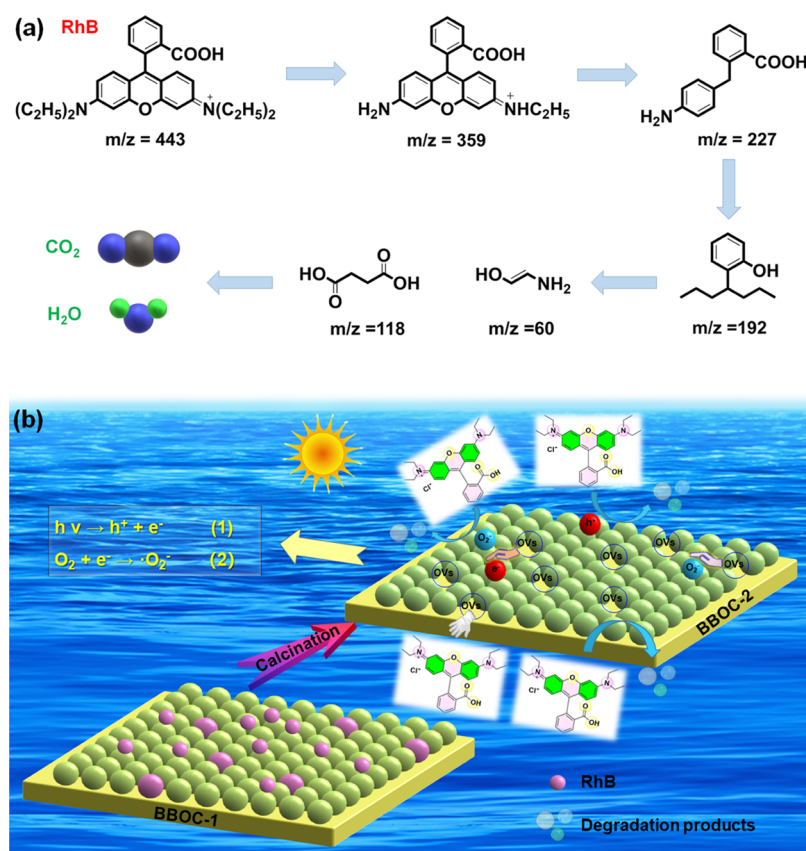
Figure 10. (a) Probable degradation pathway of RhB. (b) Schematic diagram of OV generation during calcination and the enhanced photocatalytic degradation of RhB.

suggesting a similar structural composition and good thermal stability.

3.3. Enhanced Photocatalytic Performance. The photocatalytic performances of BBOC, BBOC-1, and BBOC-2 were tested by degrading RhB under visible light ($\lambda \geq 400$ nm). As shown in Figure 8a, BBOC-2 degraded 98.23% of RhB in 40 min under visible light, exhibiting even more active performance than BBOC. Similar to BBOC and BBOC-1, the photocatalytic process can be fitted well using the first-order kinetic equation with correlation coefficients of $R^2 > 0.95$, which is in line with the first-order reaction process (Figure 8b). BBOC-2 possessed the maximum k value of 0.08087 min^{-1}, which is 1.5 and 5.7 times higher than those of BBOC (0.05228 min^{-1}) and BBOC-1 (0.01428 min^{-1}), respectively, as shown in Figure 8c.

To deepen our understanding of the enhanced photocatalytic performance of BBOC-2, EPR was conducted, and the results are shown in Figure 9. The peak at $g = 2.003$ indicated the presence of OVs in BBOC-2. OVs can be used as electron scavengers to enhance charge transfer and inhibit the recombination of e$^-$–h$^+$ pairs.[55,56] Meanwhile, OVs were important adsorption and active sites to promote the substrate reaction on the catalyst surface, which can also increase the S_{BET} of materials.[50,57]

The LC–MS analysis was applied to investigate the degradation route of RhB using BBOC-2 (Figure S2). Based on the LC–MS analysis, Figure 10b further displayed the probable degradation pathway of RhB. During the photocatalytic degradation process, RhB was decomposed into various molecular fragments gradually and was completely degraded into CO_2 and H_2O finally.[58,59]

As exhibited in Figure 10b, the adsorbed RhB was thoroughly decomposed at 350 °C under an air atmosphere, bringing part of the lattice oxygen and leaving OVs in BBOC-2.[60] Therefore, the enhanced photocatalytic activity of BBOC-2 originated from the newly generated OVs, which inhibited the recombination of photogenerated carriers and provided more active sites during visible light irradiation.

The photocatalytic performances of RhB for some recent catalysts are listed in Table S1. Our Bi_2O_3/BiOCl nanosheet exhibited high degradation efficiency, suggesting its potential application in the photocatalytic degradation of organic pollutants.

4. CONCLUSIONS

As-prepared BBOC showed photocatalytic performance toward RhB with 94.44% degradation rate in 40 min. Combined analytical techniques confirmed that the deactivation of BBOC-1 originated from the adsorbed RhB in the first run of degradation. Undecomposed RhB distributed on the surface and/or in the pores of BBOC-1, occupying active sites and then decreasing the adsorption capacities of BBOC, which finally contributed to the deactivation of BBOC. BBOC-2 was facilely activated by calcining BBOC-1 under an air atmosphere at 350 °C. BBOC-2 displayed a darker color and exhibited a more active photocatalytic performance due to the introduction of OVs, which were generated in the process of RhB decomposition. OVs provided more active sites and trapped electrons from the compounding of photogenerated

carriers during the photocatalytic process, which greatly improved the photocatalytic performance of BBOC-2 toward organic contaminants. Therefore, this study offers a reference for the investigation of the deactivation and regeneration mechanism of photocatalytic materials.

ASSOCIATED CONTENT

ⓈⒾ Supporting Information

The Supporting Information is available free of charge at https://pubs.acs.org/doi/10.1021/acsomega.2c04496.

> Investigation of the photocatalytic performance of Bi-containing catalysts; removal rate of RhB with or without a photocatalyst (Figure S1); liquid chromatography—mass spectrometry (LC—MS) spectra of photocatalytic degradation of RhB using BBOC-2 (Figure S2); photocatalytic degradation of RhB for some representative catalysts (Table S1). (PDF)

AUTHOR INFORMATION

Corresponding Author

Daoguang Teng − *School of Chemical Engineering, Zhengzhou University, Zhengzhou 450001 Henan, China; Zhongyuan Critical Metals Laboratory, Zhengzhou University, Zhengzhou 450001 Henan, China;* ⓞ orcid.org/0000-0001-9120-3070; Email: teng_daoguang@zzu.edu.cn

Authors

Peng Li − *School of Chemical Engineering, Zhengzhou University, Zhengzhou 450001 Henan, China*

Jie Qu − *School of Chemical Engineering, Zhengzhou University, Zhengzhou 450001 Henan, China*

Jing Wu − *Huaibei Blasting Technology Research Institute Co., Ltd., Huaibei 235000 Anhui, China*

Jie Zhang − *School of Ecology and Environment, Zhengzhou University, Zhengzhou 450001 Henan, China;* ⓞ orcid.org/0000-0003-4533-7056

Guoli Zhou − *School of Chemical Engineering, Zhengzhou University, Zhengzhou 450001 Henan, China*

Ying Zhang − *School of Chemical Engineering, Zhengzhou University, Zhengzhou 450001 Henan, China; Zhongyuan Critical Metals Laboratory, Zhengzhou University, Zhengzhou 450001 Henan, China*

Yijun Cao − *School of Chemical Engineering, Zhengzhou University, Zhengzhou 450001 Henan, China; Zhongyuan Critical Metals Laboratory, Zhengzhou University, Zhengzhou 450001 Henan, China;* ⓞ orcid.org/0000-0002-4635-0829

Complete contact information is available at:
https://pubs.acs.org/10.1021/acsomega.2c04496

Author Contributions

The manuscript was written through contributions of all authors. All authors have given approval to the final version of the manuscript. Conceptualization, writing—original draft, P.L.; methodology, writing—original draft, J.Q.; data curation, J.W.; investigation, J.Z.; writing—reviewing and editing, G.Z.; writing—reviewing and editing, Y.Z.; supervision, Y.C.; writing—reviewing and editing, D.T.

Notes

The authors declare no competing financial interest.

ACKNOWLEDGMENTS

REFERENCES

(1) Li, Y. J.; Dong, H. R.; Li, L.; Tang, L.; Tian, R.; Li, R.; Chen, J.; Xie, Q. Q.; Jin, Z. L.; Xiao, J. Y.; Xiao, S. J.; Zeng, G. M. Recent Advances in Waste Water Treatment through Transition Metal Sulfides-Based Advanced Oxidation Processes. *Water Res.* **2021**, *192*, No. 116850.

(2) Fattahimoghaddam, H.; Mahvelati-Shamsabadi, T.; Lee, B.-K. Efficient Photodegradation of Rhodamine B and Tetracycline over Robust and Green g-C₃N₄ nanostructures: Supramolecular Design. *J. Hazard. Mater.* **2021**, *403*, No. 123703.

(3) Kumar, A.; Venkata, K. Vacancy Engineering in Semiconductor Photocatalysts: Implications in Hydrogen Evolution and Nitrogen Fixation Applications. *Adv. Funct. Mater.* **2021**, *31*, No. 2009807.

(4) Chen, M.; Yao, J.; Huang, Y.; Gong, H.; Chu, W. Enhanced Photocatalytic Degradation of Ciprofloxacin over Bi₂O₃/(BiO)₂CO₃ Heterojunctions: Efficiency, Kinetics, Pathways, Mechanisms and Toxicity Evaluation. *Chem. Eng. J.* **2018**, *334*, 453−461.

(5) Hu, Q.; Di, J.; Wang, B.; Ji, M.; Chen, Y.; Xia, J.; Li, H.; Zhao, Y. In-Situ Preparation of NH₂-MIL-125(Ti)/BiOCl Composite with Accelerating Charge Carriers for Boosting Visible Light Photocatalytic Activity. *Appl. Surf. Sci.* **2019**, *466*, 525−534.

(6) Chen, C.; Jiang, T.; Hou, J.; Zhang, T.; Zhang, G.; Zhang, Y.; Wang, X. Oxygen Vacancies Induced Narrow Band Gap of BiOCl for Efficient Visible-Light Catalytic Performance from Double Radicals. *J. Mater. Sci. Technol.* **2022**, *114*, 240−248.

(7) Hou, J.; Dai, D.; Wei, R.; Wu, X.; Wang, X.; Tahir, M.; Zou, J. J. Narrowing the Band Gap of BiOCl for the Hydroxyl Radical Generation of Photocatalysis under Visible Light. *ACS Sustainable Chem. Eng.* **2019**, *7*, 16569−16576.

(8) Hou, J.; Zhang, T.; Jiang, T.; Wu, X.; Zhang, Y.; Tahir, M.; Hussain, A.; Luo, M.; Zou, J.; Wang, X. Fast Preparation of Oxygen Vacancy-Rich 2D/2D Bismuth Oxyhalides-Reduced Graphene Oxide Composite with Improved Visible-Light Photocatalytic Properties by Solvent-Free Grinding. *J. Cleaner Prod.* **2021**, *328*, No. 129651.

(9) Song, T.; Xie, C.; Matras-Postolek, K.; Yang, P. 2D Layered g-C₃N₄/WO₃/WS₂ S-Scheme Heterojunctions with Enhanced Photochemical Performance. *J. Phys. Chem. C* **2021**, *125*, 19382−19393.

(10) Guo, J.; Shen, C. H.; Sun, J.; Xu, X. J.; Li, X. Y.; Fei, Z. H.; Liu, Z. T.; Wen, X. J. Highly Efficient Activation of Peroxymonosulfate by Co₃O₄/Bi₂MoO₆ p-n Heterostructure Composites for the Degradation of Norfloxacin under Visible Light Irradiation. *Sep. Purif. Technol.* **2021**, *259*, No. 118109.

(11) Wang, J. C.; Wang, J.; Li, N. Y.; Du, X. Y.; Ma, J.; He, C. H.; Li, Z. Q. Direct Z-Scheme 0D/2D Heterojunction of CsPbBr₃ Quantum Dots/Bi₂WO₆ Nanosheets for Efficient Photocatalytic CO₂ Reduction. *ACS Appl. Mater. Interfaces* **2020**, *12*, 31477−31485.

(12) Niu, X. H.; Bai, X. W.; Zhou, Z. B.; Wang, J. L. Rational Design and Characterization of Direct Z-Scheme Photocatalyst for Overall Water Splitting from Excited State Dynamics Simulations. *ACS Catal.* **2020**, *10*, 1976−1983.

(13) Wen, X. J.; Qian, L.; Lv, X. X.; Sun, J.; Guo, J.; Fei, Z. H.; Niu, C. G. Photocatalytic Degradation of Sulfamethazine Using a Direct Z-Scheme AgI/Bi₄V₂O₁₁ Photocatalyst: Mineralization Activity, Degra-

dation Pathways and Promoted Charge Separation Mechanism. *J. Hazard. Mater.* 2020, *385*, No. 121508.

(14) He, F.; Meng, A. Y.; Cheng, B.; Ho, W. K.; Yu, J. G. Enhanced Photocatalytic H_2-Production Activity of WO_3/TiO_2 Step-Scheme Heterojunction by Graphene Modification. *Chin. J. Catal.* 2020, *41*, 9−20.

(15) Xia, P. F.; Cao, S. W.; Zhu, B. C.; Liu, M. J.; Shi, M. S.; Yu, J. G.; Zhang, Y. F. Designing a 0D/2D S-Scheme Heterojunction over Polymeric Carbon Nitride for Visible-Light Photocatalytic Inactivation of Bacteria. *Angew. Chem., Int. Ed.* 2020, *59*, 5218−5225.

(16) He, F.; Zhu, B. C.; Cheng, B.; Yu, J. G.; Ho, W. K.; Macyk, W. 2D/2D/0D TiO_2/C_3N_4/Ti_3C_2 MXene Composite S-Scheme Photocatalyst with Enhanced CO_2 Reduction Activity. *Appl. Catal., B* 2020, *272*, No. 119006.

(17) Chai, S. Y.; Kim, Y. J.; Jung, M. H.; Chakraborty, A. K.; Jung, D.; Lee, W. I. Heterojunctioned $BiOCl$/Bi_2O_3, a New Visible Light Photocatalyst. *J. Catal.* 2009, *262*, 144−149.

(18) Tang, X.; Ma, C.; Liu, N.; Liu, C.; Liu, S. Visible Light β-Bi_2O_3/$BiOCl$ Heterojunction Photocatalyst with Highly Enhanced Photocatalytic Activity. *Chem. Phys. Lett.* 2018, *709*, 82−87.

(19) Kong, S.; An, Z.; Zhang, W.; An, Z.; Yuan, M.; Chen, D. Preparation of Hollow Flower-Like Microspherical β-Bi_2O_3/$BiOCl$ Heterojunction and High Photocatalytic Property for Tetracycline Hydrochloride Degradation. *Nanomaterials* 2020, *10*, No. 57.

(20) Nagar, A.; Basu, S. Fabrication of 3D Porous Peony Flower-Like β-Bi_2O_3/$BiOCl$ Heterostructure for Synergistically Boosting the Visible-Light-Driven Degradation of Organic Pollutants. *Environ. Technol. Innovation* 2021, *24*, No. 101956.

(21) Cha, B. J.; Saqlain, S.; Seo, H. O.; Kim, Y. D. Hydrophilic Surface Modification of TiO_2 to Produce a Highly Sustainable Photocatalyst for Outdoor Air Purification. *Appl. Surf. Sci.* 2019, *479*, 31−38.

(22) Stefanov, B. I.; Niklasson, G. A.; Granqvist, C. G.; Österlund, L. Gas-Phase Photocatalytic Activity of Sputter-Deposited Anatase TiO_2 Films: Effect of (001) Preferential Orientation, Surface Temperature And Humidity. *J. Catal.* 2016, *335*, 187−196.

(23) Mamaghani, A. H.; Haghighat, F.; Lee, C.-S. Photocatalytic Oxidation Technology for Indoor Environment Air Purification: The State-of-the-Art. *Appl. Catal., B* 2017, *203*, 247−269.

(24) Yang, C. T.; Miao, G.; Pi, Y. H.; Xia, Q. B.; Wu, J. L.; Li, Z.; Xiao, J. Abatement of Various Types of VOCs by Adsorption/Catalytic Oxidation: A Review. *Chem. Eng. J.* 2019, *370*, 1128−1153.

(25) Zhang, G. X.; Liu, Y. Y.; Zheng, S. L.; Hashisho, Z. Adsorption of Volatile Organic Compounds onto Natural Porous Minerals. *J. Hazard. Mater.* 2019, *364*, 317−324.

(26) Weon, S.; Choi, W. TiO_2 Nanotubes with Open Channels as Deactivation-Resistant Photocatalyst for the Degradation of Volatile Organic Compounds. *Environ. Sci. Technol.* 2016, *50*, 2556−2563.

(27) Weon, S.; He, F.; Choi, W. Status and Challenges in Photocatalytic Nanotechnology for Cleaning Air Polluted with Volatile Organic Compounds: Visible Light Utilization and Catalyst Deactivation. *Environ. Sci.: Nano* 2019, *6*, 3185−3214.

(28) Long, X.; Feng, C.; Ding, D.; Chen, N.; Yang, S.; Chen, H.; Wang, X.; Chen, R. Oxygen Vacancies-Enriched $CoFe_2O_4$ for Peroxymonosulfate Activation: The Reactivity between Radical-Nonradical Coupling Way and Bisphenol A. *J. Hazard. Mater.* 2021, *418*, No. 126357.

(29) Han, X.; Chen, T.; Li, R.; Cheng, F.; Zhang, M.; Guo, M. Hydrothermal Temperature Effect on Microstructure Evolution and Fenton-Like Catalytic Performance of Spinel Ferrite (Mg,Ni)-(Fe,Al)$_2$O$_4$ Synthesized from Saprolitic Nickel Laterite. *Colloids Surf., A* 2019, *568*, 11−19.

(30) Wang, L.; Wang, Y.; Cheng, Y.; Liu, Z.; Guo, Q.; Ha, M. N.; Zhao, Z. Hydrogen-Treated Mesoporous WO_3 as a Reducing Agent of CO_2 to Fuels (CH_4 and CH_3OH) with Enhanced Photothermal Catalytic Performance. *J. Mater. Chem. A* 2016, *4*, 5314−5322.

(31) Wang, J.; Xia, Y.; Zhao, H.; Wang, G.; Xiang, L.; Xu, J.; Komarneni, S. Oxygen Defects-Mediated Z-Scheme Charge Separation in g-C_3N_4/ZnO Photocatalysts for Enhanced Visible-Light

(32) Wang, L.; Liu, G.; Wang, B.; Chen, X.; Wang, C.; Lin, Z.; Xia, J.; Li, H. Oxygen Vacancies Engineering−Mediated $BiOBr$ Atomic Layers for Boosting Visible Light-Driven Photocatalytic CO_2 Reduction. *Sol. RRL* 2020, *5*, No. 2000480.

(33) Priya, B.; Raizada, P.; Singh, N.; Thakur, P.; Singh, P. Adsorptional Photocatalytic Mineralization of Oxytetracycline and Ampicillin Antibiotics Using Bi_2O_3/$BiOCl$ Supported on Graphene Sand Composite and Chitosan. *J. Colloid Interface Sci.* 2016, *479*, 271−283.

(34) Bera, K. K.; Majumdar, R.; Chakraborty, M.; Bhattacharya, S. K. Phase Control Synthesis of α, β and α/β Bi_2O_3 Hetero-Junction with Enhanced and Synergistic Photocatalytic Activity on Degradation of Toxic Dye, Rhodamine-B under Natural Sunlight. *J. Hazard. Mater.* 2018, *352*, 182−191.

(35) Chen, J.; Zhong, J.; Li, J.; Qiu, K. Boosted Photocatalytic Removal of Tetracycline on S-Scheme $Bi_{12}O_{17}Cl_2$/α-Bi_2O_3 Heterojunctions with Rich Oxygen Vacancies. *Appl. Surf. Sci.* 2021, *563*, No. 150246.

(36) Din, S. T. U.; Lee, H.; Yang, W. Z-Scheme Heterojunction of 3-Dimensional Hierarchical Bi_3O_4Cl/Bi_5O_7I for a Significant Enhancement in the Photocatalytic Degradation of Organic Pollutants (RhB and BPA). *Nanomaterials* 2022, *12*, No. 767.

(37) Priya, B.; Raizada, P.; Singh, N.; Thakur, P.; Singh, P. Adsorptional Photocatalytic Mineralization of Oxytetracycline and Ampicillin Antibiotics Using Bi_2O_3/$BiOCl$ Supported on Graphene Sand Composite and Chitosan. *J. Colloid Interface Sci.* 2016, *479*, 271−283.

(38) Yuan, Q.; Wei, S.; Hu, T.; Ye, Y.; Cai, Y.; Liu, J.; Li, P.; Liang, C. Defect-Modified Ultrathin $BiOX$ (X = Cl, Br) Nanosheets Via a Top-Down Approach with Effective Visible-Light Photocatalytic Degradation. *J. Phys. Chem. C* 2021, *125*, 18630−18639.

(39) Liu, C.; Ren, X.; Lin, F.; Fu, X.; Lin, X.; Li, T.; Sun, K.; Huang, J. Structure of the Au_{23}−$xAgx(S-Adm)_{15}$ Nanocluster and its Application for Photocatalytic Degradation of Organic Pollutants. *Angew. Chem.* 2019, *131*, 11457−11461.

(40) Yang, H.; Zheng, F.; Liu, F.; Lin, L.; Huang, X.; Lin, Y.; Li, S. Positively and Negatively Charged Double Shell with Au Sandwich for Protecting and Enhancing Photocatalytic Activity of TiO_2-Based Photocatalyst. *J. Phys. Chem. C* 2021, *125*, 23729−23735.

(41) Huang, S.; Wu, Y.; Zhang, Q.; Jin, X.; Li, D.; Liu, H.; Chen, P.; Lv, W.; Liu, G. $Bi_2O_2CO_3$/Bi_2O_3 Z-Scheme Photocatalyst with Oxygen Vacancies and Bi for Enhanced Visible-Light Photocatalytic Degradation of Tetracycline. *Environ. Sci.: Nano* 2022, *9*, 2104−2120.

(42) Loo, W. W.; Pang, Y. L.; Lim, S.; Wong, K. H.; Lai, C. W.; Abdullah, A. Z. Enhancement of Photocatalytic Degradation of Malachite Green Using Iron Doped Titanium Dioxide Loaded on Oil Palm Empty Fruit Bunch-Derived Activated Carbon. *Chemosphere* 2021, *272*, No. 129588.

(43) Cai, Z.; Huang, Y.; Ji, H.; Liu, W.; Fu, J.; Sun, X. Type-II Surface Heterojunction of Bismuth-Rich $Bi_4O_5Br_2$ on Nitrogen-Rich g-C_3N_5 Nanosheets for Efficient Photocatalytic Degradation of Antibiotics. *Sep. Purif. Technol.* 2022, *280*, No. 119772.

(44) Zhang, Z.; Zhang, Y.; Li, Z.; Yang, X.; Yang, X.; Peng, Y.; Yu, J. Preparation, Characterization and Application of Epitaxial Grown $BiOBr$ (110) Film on $ZnFe_2O_4$ Surface with Enhanced Photocatalytic Fenton Oxidation Properties. *Nanomaterials* 2022, *12*, No. 1508.

(45) Mei, J.; Tao, Y.; Gao, C.; Zhu, Q.; Zhang, H.; Yu, J.; Fang, Z.; Xu, H.; Wang, Y.; Li, G. Photo-Induced Dye-Sensitized $BiPO_4$/$BiOCl$ System for Stably Treating Persistent Organic Pollutants. *Appl. Catal., B* 2021, *285*, No. 119841.

(46) Wu, X.; Zeng, Y.; Liu, H.; Zhao, J.; Zhang, T.; Wang, S. L. Noble-Metal-Free Dye-Sensitized Selective Oxidation of Methane to Methanol with Green Light (550 nm). *Nano Res.* 2021, *14*, 4584−4590.

(47) Huang, H.; Li, Y. X.; Jiang, G. J.; Wang, H. L.; Jiang, W. F. In situ construction of Dye-Sensitized $BiOCl$/Rutile-TiO_2 Nanorod Heterojunctions with Highly Enhanced Photocatalytic Activity for

Treating Persistent Organic Pollutants. *Inorg. Chem.* **2021**, *60*, 17325−17338.

(48) Udrescu, A.; Florica, S.; Chivu, M.; Mercioniu, I.; Matei, E.; Baibarac, M. Rhodamine B Photodegradation in Aqueous Solutions Containing Nitrogen Doped TiO_2 and Carbon Nanotubes Composites. *Molecules* **2021**, *26*, No. 7237.

(49) Liu, D.; Chen, D.; Li, N.; Xu, Q.; Li, H.; He, J.; Lu, J. Surface Engineering of $g-C_3N_4$ by Stacked BiOBr Sheets Rich in Oxygen Vacancies for Boosting Photocatalytic Performance. *Angew. Chem., Int. Ed.* **2020**, *59*, 4519−4524.

(50) Wu, S. J.; Xiong, J. W.; Sun, J. G.; Hood, Z. D.; Zeng, W.; Yang, Z. Z.; Gu, L.; Zhang, X. X.; Yang, S. Z. Hydroxyl-Dependent Evolution of Oxygen Vacancies Enables the Regeneration of BiOCl Photocatalyst. *ACS Appl. Mater. Interfaces* **2017**, *9*, 16620−16626.

(51) Shiraishi, Y.; Hashimoto, M.; Chishiro, K.; Moriyama, K.; Tanaka, S.; Hirai, T. Photocatalytic Dinitrogen Fixation with Water on Bismuth Oxychloride in Chloride Solutions for Solar-to-Chemical Energy Conversion. *J. Am. Chem. Soc.* **2020**, *142*, 7574−7583.

(52) Zhang, S.; Chen, J.; Jia, Q.; Jiang, Q.; Yan, J.; Yang, G. A Novel and Effective Recyclable BiOCl/BiOBr Photocatalysis for Lignin Removal from Pre-Hydrolysis Liquor. *Nanomaterials* **2021**, *11*, No. 2836.

(53) Shekh, M. I.; Amirian, J.; Du, B.; Kumar, A.; Sharma, G.; Stadler, F. J.; Song, J. Electrospun ferric ceria nanofibers blended with MWCNTs for high-performance electrochemical detection of uric acid. *Ceram. Int.* **2020**, *46*, 9050−9064.

(54) Dhiman, P.; Kumar, A.; Shekh, M.; Sharma, G.; Rana, G.; Vo, D. V. N.; AlMasoud, N.; Naushad, M.; ALOthman, Z. A. Robust magnetic $ZnO-Fe_2O_3$ Z-scheme hetereojunctions with in-built metal-redox for high performance photo-degradation of sulfamethoxazole and electrochemical dopamine detection. *Environ. Res.* **2021**, *197*, No. 111074.

(55) Yu, H. B.; Ge, D.; Liu, Y. P.; Lu, Y.; Wang, X. H.; Huo, M. X.; Qin, W. C. One-Pot Synthesis of BiOCl Microflowers Co-Modified with Mn and Oxygen Vacancies for Enhanced Photocatalytic Degradation of Tetracycline under Visible Light. *Sep. Purif. Technol.* **2020**, *251*, No. 117414.

(56) ElMetwally, A. E.; Sayed, M. S.; Zeynaloo, E.; Zahran, E. M.; Shim, J. J.; Knecht, M. R.; Bachas, L. G. Hierarchical Core-Shell ACOF-1@BiOBr as an Efficient Photocatalyst for the Degradation of Emerging Organic Contaminants. *J. Phys. Chem. C* **2022**, *126*, 2503−2516.

(57) Hou, J. H.; Dai, D.; Wei, R.; Wu, X. G.; Wang, X. Z.; Tahir, M.; Zou, J. J. Narrowing the Band Gap of BiOCl for the Hydroxyl Radical Generation of Photocatalysis under Visible Light. *ACS Sustainable Chem. Eng.* **2019**, *7*, 16569−16576.

(58) Kang, Z.; Qin, N. I.; Lin, E.; Wu, J.; Yuan, B.; Bao, D. Effect of Bi_2WO_6 Nanosheets on the Ultrasonic Degradation of Organic Dyes: Roles of Adsorption and Piezocatalysis. *J. Cleaner Prod.* **2020**, *261*, No. 121125.

(59) Taniguchi, T.; Nurdiwijayanto, L.; Li, S.; Lim, H.; Miyata, Y.; Lu, X.; Ma, R.; Tang, D.; Ueda, S.; Tsukagoshi, K.; Sasaki, T.; Osada, M. On/Off Boundary of Photocatalytic Activity between Single-and Bilayer MoS_2. *ACS Nano* **2020**, *14*, 6663−6672.

(60) Niu, S. Y.; Zhang, R. Y.; Guo, C. F. Oxygen Vancancy Induced Superior Visible-Light Driven Photocatalytic Performance in the BiOCl Homojunction. *Mater. Chem. Front.* **2020**, *10*, 1039−1049.